Near-Surface $^{125}Te^+$ Spins with Millisecond Coherence Lifetime

Mantas Šimėnas,[1] James O'Sullivan,[1] Oscar W. Kennedy,[1] Sen Lin,[2] Sarah Fearn,[3] Christoph W. Zollitsch,[1] Gavin Dold,[1] Tobias Schmitt,[4] Peter Schüffelgen,[4] Ren-Bao Liu,[2] and John J. L. Morton[1,5,*]

[1]*London Centre for Nanotechnology, UCL, 17-19 Gordon Street, London WC1H 0AH, United Kingdom*
[2]*Department of Physics, Centre for Quantum Coherence and The Hong Kong Institute of Quantum Information Science and Technology, The Chinese University of Hong Kong, Hong Kong, China*
[3]*Department of Materials, Imperial College London, London SW7 2BX, United Kingdom*
[4]*Institute for Semiconductor Nanoelectronics, Peter Grünberg Institute 9, Forschungszentrum Jülich and RWTH Aachen University, 52425 Jülich, Germany*
[5]*Department of Electrical and Electronic Engineering, UCL, Malet Place, London WC1E 7JE, United Kingdom*

(Received 24 September 2021; revised 11 March 2022; accepted 20 July 2022; published 9 September 2022)

Impurity spins in crystal matrices are promising components in quantum technologies, particularly if they can maintain their spin properties when close to surfaces and material interfaces. Here, we investigate an attractive candidate for microwave-domain applications, the spins of group-VI $^{125}Te^+$ donors implanted into natural Si at depths as shallow as 20 nm. We show that surface band bending can be used to ionize such near-surface Te to spin-active Te^+ state, and that optical illumination can be used further to control the Te donor charge state. We examine spin activation yield, spin linewidth, and relaxation (T_1) and coherence times (T_2) and show how a zero-field 3.5 GHz "clock transition" extends spin coherence times to over 1 ms, which is about an order of magnitude longer than other near-surface spin systems.

DOI: 10.1103/PhysRevLett.129.117701

Donor spins in nanoscale silicon devices have been shown to be a promising building block for various solid state quantum devices, including atomic qubits [1] and quantum memories with coherence times approaching seconds [2]. Such devices typically contain band discontinuities at silicon-metal and silicon-vacuum interfaces that build electric fields into devices, impacting the charge and spin state of nearby donors. Placing donors close to these interfaces is often important, for example, to increase spin-resonator coupling [3], or couple donor spins to electrostatically tunable quantum dots [4,5]. Without control of the surface potential (for example, through a metallic top gate), this typically limits the minimum donor-interface distance to tens of nanometers for shallow group-V donor electron spins [6], whereas deeper donors could be placed closer to electrodes. There is also evidence that, for deeper donors, the electron spin coherence is less strongly influenced by naturally abundant ^{29}Si spins (as seen by comparing results from P and Bi donors [7,8]).

Singly ionized group-VI chalcogens (S^+, Se^+, and Te^+) possess an electron spin $S = 1/2$, like the group-V donors, but have much larger ionisation energies [9–11]. These donors have attracted recent interest due to their optical transitions [12]. Through continuous-wave electron spin resonance (ESR) studies [9,13], $^{125}Te^+$ in silicon is known to have a large isotropic hyperfine coupling of ~3.5 GHz to the ^{125}Te nuclear spin ($I = 1/2$). Singly ionized double donors such as $^{125}Te^+$ therefore offer a potential route to maintaining a donor electron spin close to a silicon surface or interface, combined with the presence of a microwave clock transition [14] at zero magnetic field.

Another critical challenge encountered when placing electron spins very close to the surface is spin decoherence caused by fluctuating surface defects [15,16]. For example, the coherence time of negatively charged nitrogen-vacancy centers in diamond drops from a few hundred to tens of microseconds when the surface is approached, significantly limiting sensitivity of nitrogen-vacancy centers for nanoscale spin detection and imaging [16–18]. This stimulates the search for other near-surface electron spin centers that are less sensitive to surface-induced decoherence.

Here, we present pulsed ESR measurements of $^{125}Te^+$ implanted at depths of 20 and 300 nm in natural silicon. We investigate two different methods to singly ionize ^{125}Te—first by codoping with boron for deep-implanted donors, and second by directly exploiting the band bending arising from Fermi level pinning (FLP) for near-surface donors. We demonstrate superior coherence times of more than 1 ms for near-surface spins as the zero-field clock transition is approached. We also show how infrared illumination of the shallow-implanted sample improves

Published by the American Physical Society under the terms of the Creative Commons Attribution 4.0 International license. Further distribution of this work must maintain attribution to the author(s) and the published article's title, journal citation, and DOI.

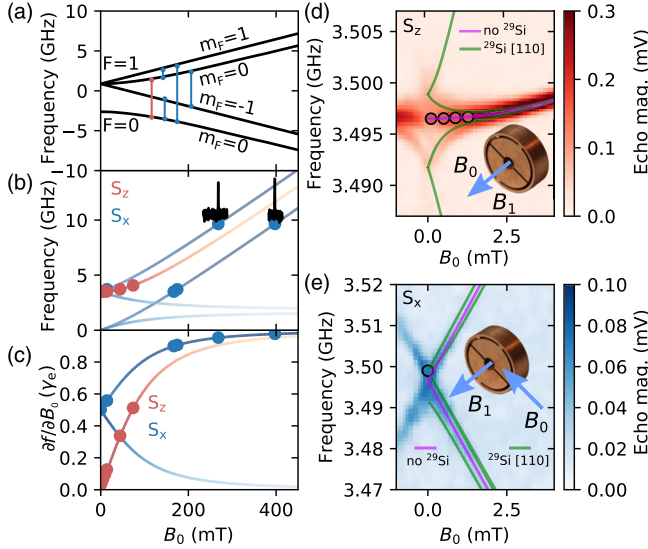

FIG. 1. (a) Spin eigenenergies of ^{125}Te$^+$:Si with S_x and S_z transitions marked in blue and red, respectively. (b) Frequencies of allowed spin transitions, where the line intensity is proportional to the transition probability. Echo-detected spectra obtained at 9.65 GHz are shown in black. (c) First order magnetic field dependence of the transition frequencies. (d),(e) Echo-detected spectra of ^{125}Te$^+$:Si close to zero magnetic field with the cavity oriented to measure (d) S_z and (e) S_x transitions. Solid lines show simulations assuming only a hyperfine constant of 3.4965 GHz to ^{125}Te nucleus, or, in addition, a superhyperfine (SHF) interaction with a neighboring [110]-shell ^{29}Si nuclear spin. All measurements are taken at 10 K. Circles in (b)–(e) show fields and transitions, where T_2 measurements are performed.

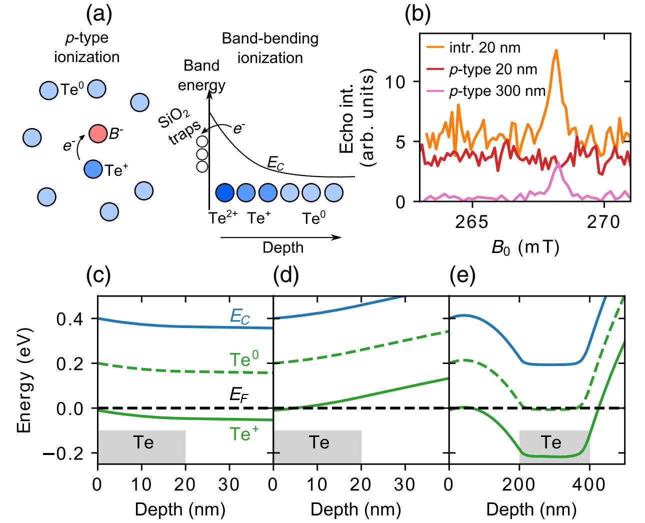

FIG. 2. (a) Cartoons showing the different ionisation mechanisms of Te in silicon. (b) EDFSs performed at X band for S_x transitions. (c)–(e) Simulated band profiles for the three samples used in this study assuming FLP of 0.4 eV below the conduction band. The simulation results are consistent with EDFSs in (b). (c) Intrinsic wafer with 20 keV implant energy gives all Te singly ionized by surface band bending. (d) p-type wafer with 20 keV implant energy has approximately all Te doubly ionized. (e) p-type wafer with 800 keV implant energy has the Fermi level close to the singly ionized Te level as 1/10 of Te atoms are ionized by sacrificing an electron to the boron acceptors present at 1/10 the density of Te.

the ionization fraction, surpassing that achieved by codoping.

The singly ionized ^{125}Te donor has a single bound electron ($S = 1/2$) coupled to the ^{125}Te nuclear spin ($I = 1/2$) via an isotropic hyperfine coupling A (see Supplemental Material [19] for spin Hamiltonian details). Figures 1(a) and 1(b) show the calculated spin transition frequencies (f) and probabilities of ^{125}Te$^+$:Si as a function of magnetic field, neglecting the superhyperfine (SHF) term. Transitions are labeled S_z ($\Delta m_F = 0$) or S_x ($\Delta m_F = \pm 1$), which are, respectively, driven when the microwave magnetic field component is applied parallel or perpendicular to the static magnetic field. Here, m_F denotes the projection of the quantum number $F = S \pm I$. The ESR experiments described below were performed using a copper loop-gap resonator with adjusted orientation depending on the type of the transition, as shown in the insets to Figs. 1(d) and 1(e) (see Supplemental Material [19] for details).

The first derivative of the transition frequency with respect to the applied field, $\partial f/\partial B_0$, is an important parameter in determining spin coherence lifetimes and inhomogeneous broadening. So-called clock transitions, where $\partial f/\partial B_0 = 0$, possess extended coherence times [14,25–28] and narrow linewidths [14,28]. Like any isotropically coupled spin system, ^{125}Te$^+$ exhibits an S_z clock transition at zero field [see Fig. 1(c)]. Because of the large hyperfine coupling, the clock transition of ^{125}Te$^+$ occurs in the microwave domain at 3.4965 GHz. In Figs. 1(d) and 1(e) we present echo-detected field sweeps (EDFS) of deep-implanted sample for S_z and S_x transitions, respectively, while varying the frequency of the microwave drive about 3.5 GHz. We resolve the main spin transition as well as the SHF levels, revealing perfect agreement with the calculated transition frequency.

To be spin active, chalcogens must be incorporated into the silicon lattice (as with group-V donors) and also be singly ionized [10,11]. Using the deep-implanted p-type sample, we first investigated three annealing schedules (5 minutes at 600, 800, and 1000 °C in dry nitrogen) to incorporate ^{125}Te into the lattice after implantation. In these samples, ionisation is achieved by codoping ^{125}Te ion implanted at 800 keV to a depth of 300 nm with a peak concentration of 10^{17} cm^{-3} (profile shown in Supplemental Material [19]) with boron at a concentration of $2.4(2) \times 10^{16}$ cm^{-3} [Fig. 2(a)]. Using an excess of Te, we aim to ionize the majority of the boron into an electron spinless B^- state to reduce the impact on the Te$^+$ donor spin coherence through spectral diffusion. This necessarily reduces the fraction of Te$^+$ compared to the overall quantity of implanted Te.

Spin echo measurements at 9.65 GHz show two resonances at the expected magnetic field positions for the S_x transitions shown in Fig. 1(b). By comparing these echo amplitudes to a reference P:Si sample (see Supplemental Material [19] for details), we determined the activation yield of Te^+. We observed that activation yield increases from ~15% to 22% with annealing temperature increasing from 600 to 1000 °C (see Table S1 in Supplemental Material [19]). Given that the ionization mechanism is the same between the samples (B codoping), we attribute this change to a higher Te incorporation fraction. We also observed that the electron spin coherence time T_2 obtained at X band increases with annealing temperature (Table S1), likely due to healing of spin-active implantation damage at higher annealing temperature.

We also implanted intrinsic silicon at a depth of 20 nm using 20 keV implantation energy (SIMS profiles in the Supplemental Material [19]) and used surface band bending at the silicon-vacuum interface caused by FLP to ionize Te close to the surface, as shown schematically in Fig. 2(a). Band bending is a ubiquitous effect and also occurs due to Schottky barriers at silicon-metal interfaces and can be controlled by surface treatments [29]. The EDFS traces in Fig. 2(b) confirm the generation of Te^+ in the shallow-implanted intrinsic sample (as well as the deep-implanted p-type silicon), but there is no signal from the shallow-implanted p-type sample. Note that the number of spins of the shallow-implanted intrinsic sample is much lower compared to the deep-implanted samples (Table S1), resulting in a much weaker ESR signal.

In order to understand the ESR signal strength in the different samples, we self-consistently solved the Schrödinger-Poisson equation in one dimension [30] and simulated different implants and substrates with various FLP levels. FLPs in the range of 0.4–0.5 eV give ionization profiles consistent with the echo amplitudes in Fig. 2(b) and are in line with literature values for FLP at the silicon-silicon oxide interface [31]. We show simulations of the band profiles with FLP at 0.4 eV below the conduction band in Figs. 2(c)–2(e). Figure 2(c) shows simulated band profiles of 10^{17} cm^{-3} Te extending 20 nm into intrinsic silicon, where all Te is singly ionized. However, for the shallow-implanted p-type material [Fig. 2(d)] the simulation predicts predominantly ESR-silent $^{125}Te^{2+}$, consistent with the lack of observed spin echo from this sample [Fig. 2(b)]. Finally, in the simulation of deep-implanted Te into p-type Si [Fig. 2(e)] the Fermi level is close to the Te^+ level, resulting in Te ionization commensurate with the boron codoping concentration. See Supplemental Material [19] for extended simulations.

A comparison with the P:Si reference sample gives an estimated Te activation of ~7% for the shallow-implanted sample (Table S1), which arises from a combination of imperfect incorporation of Te into the lattice and less than 100% ionization into Te^+. Shining light of different

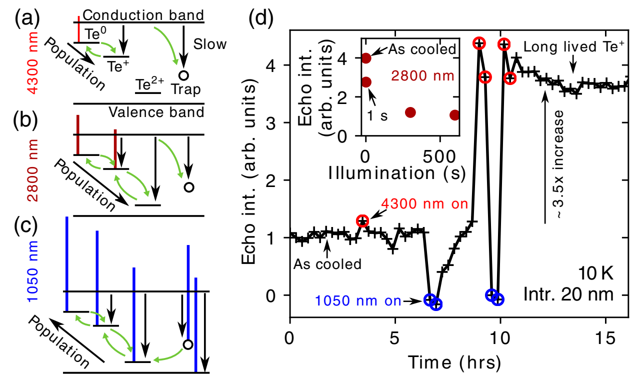

FIG. 3. Energy levels and electron transitions of Te:Si under illumination of (a) 4300 nm, (b) 2800 nm, and (c) 1050 nm light. The labels of energy levels are marked in (a). Colored vertical lines show the energy of incident photons supplied by LEDs at cryogenic temperatures and indicate which levels are excited by these photons. Vertical arrows show electron capture. Green arrows indicate population swapping between levels under illumination with arrow direction indicating the shift of population of Te donors under illumination. (d) Echo intensity from the shallow-implanted intrinsic sample as a function of time as LEDs are shone at the sample during the echo acquisition (red and blue circles) at 10 K. The inset shows the echo integral as a function of cumulative 2800 nm illumination showing that the echo is suppressed.

wavelengths at this sample allows us to alter the charge configuration and improve the fraction of Te^+. We explore illumination at three different wavelengths: 1050 nm, sufficient to excite carriers across the Si band gap; 2800 nm, sufficient to promote electrons from Te^+ or Te^0 to the conduction band; and 4300 nm, which excites only the Te^0 state [see Figs. 3(a)–3(c)]. Illumination at 2800 nm drives the formation of (spinless) Te^{2+}, as illustrated by the fourfold reduction of echo intensity shown in the inset of Fig. 3(d).

In Fig. 3(d) we explore the effects of 4300 nm and 1050 nm illumination, with respect to the initial echo intensity from the sample as cooled from room temperature to 10 K. Illumination first with 4300 nm results in a small (~20%) increase in echo intensity, indicating there is only a small concentration of Te^0 in the as-cooled state, consistent with our simulations above. Subsequent illumination at 1050 nm results in a complete suppression of the electron spin echo, consistent with driving population from Te^+ (and Te^{2+}) into the neutral Te^0 state. The echo recovered on the timescale of an hour, due to some redistribution of population from Te^0 to Te^+, similar to Se^+ recovery after illumination by 1047 nm [10]. However, as is evident from the large (3.5×) increase in echo intensity following subsequent illumination at 4300 nm, there remained a substantial fraction of Te^0, much greater than that present upon cooling the sample. Further rounds of illumination at 1050 and 4300 nm demonstrate the ability to switch between Te^0 and Te^+ states. The nonequilibrium Te^+

population created persists for at least ~16 h (further data off panel) and represents a spin-activation fraction of ~26%. Similar illumination experiments applied to the deep-implanted p-type sample are described in the Supplemental Material [19]; however, no increase in echo intensity was observed relative to the as-cooled state.

The linewidths (half width at half maximum) of the S_x and S_z transitions of the deep-implanted p-type sample largely follow $\partial f/\partial B_0$, as shown in Fig. S6A, consistent with inhomogeneous broadening from ^{29}Si nuclear spins, as is commonly seen for donors in natural silicon. The linewidth reaches a minimum value of ~0.6 MHz (Fig. S6B), which is close to the pulse bandwidth limit (π-pulse duration 140 ns), but approximately equal to that measured for a clock transition in Bi:^{nat}Si doped at similar concentration [32]. The line shape is well fit by a single Gaussian (see Fig. S6B) with no evidence of additional splitting caused by isotope mass variation of the nearest-neighbor silicon atoms [33]—the low ($I = 1/2$) nuclear spin of ^{125}Te means that the spin transitions are typically less sensitive to shifts in the hyperfine coupling than donors with high-spin nuclei like ^{209}Bi. The increase in line broadening for $\partial f/\partial B_0 \lesssim 0.03$ (corresponding to $B_0 \lesssim 4$ mT) is due to SHF transitions splitting from the main transition as zero magnetic field is approached (see Supplemental Material [19] for details).

Next, we studied the spin relaxation time, T_1, and spin coherence time, T_2, in the temperature range 6.5–18 K for an S_x transition at 9.65 GHz and close to the S_z clock transition (see Figs. S10 and S11). In both cases, we observed the $T_1 \propto T^{-9}$ temperature dependence indicating a (phonon-induced) Raman spin-relaxation process, as was also observed for ^{77}Se$^+$ in ^{28}Si [10]. For temperatures above about 10 K, T_2 is limited by T_1; however, below 8 K, T_2 reaches a constant value.

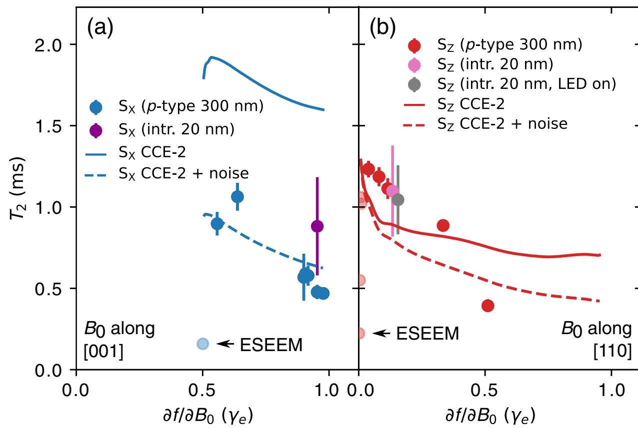

FIG. 4. T_2 as a function of $\partial f/\partial B_0$ for (a) S_x and (b) S_z transitions and different measurement conditions and samples. Points where T_2 is suppressed by ESEEM are indicated with increased transparency. The solid curves mark the limit to T_2 considering nuclear spin dynamics as a function of electron spin $\partial f/\partial B_0$. Adding in the effects of classical magnetic field noise gives good agreement to experiment (dashed curves).

We investigate T_2 in this low-temperature limit for both S_x and S_z transitions in more detail, examining the effect of $\partial f/\partial B_0$. The results are summarized in Fig. 4, including results from both the shallow- and deep-implanted samples. We can expect that the naturally abundant ^{29}Si nuclear spins in these samples pose a limit on the measured coherence times, which can be calculated using the cluster correlation expansion (CCE) method [34], as used for (shallower) group-V donors [7,8]. We plot this calculated limit (CCE-2, based on two-body correlations of bath spins) along with the experimental results in Fig. 4, with further details of the CCE simulations provided in the Supplemental Material [19].

From the T_2 measurements and simulations, we make four observations. First is that the T_2 measured for the shallow-implanted Te$^+$ in intrinsic substrate (ionized by surface band bending) reaches above 1 ms and is the same as for the deep-implanted Te$^+$ in p-type substrate (ionised by the boron acceptors). This suggests that neither the effect of the compensation nor proximity to the surface limit the measured T_2 values (see Supplemental Material [19] for details).

Second, the T_2 values of the S_x transitions are longer compared to the S_z transitions at the same $\partial f/\partial B_0$. This difference occurs due to different sample orientation with respect to B_0 direction when measuring the S_x (B_0 along [001]) and S_z (along [110]) transitions [35] (see Supplemental Material [19] for details).

The third observation is that the T_2 limit from the ^{29}Si nuclear spin bath predicted by the CCE-2 calculations is almost a factor of 2 longer than that seen for the shallow donors such as Bi and P [7,8]. However, as a result, the nuclear spin bath alone does not appear to account for the observed T_2 values [see solid curves in Fig. 4(a).] We consider additional sources of decoherence such as unhealed damage from ion implantation and spin concentration effects in the Supplemental Material [19] and conclude that they are unlikely to play a significant role in these measurements. It is known that experimental setups similar to that used here suffer from magnetic field noise that typically limits the measured T_2 to ~1 ms. This effect can be circumvented by performing single-shot measurements of echo magnitude [36], but this requires a large signal-to-noise ratio not available when measuring implanted samples using 3D cavities. Such an additional magnetic-field-type decoherence process (rate $\propto \partial f/\partial B_0$) with a corresponding $T_2 = 1$ ms for $\partial f/\partial B_0 = \gamma_e$ is able to rather well reproduce the observed measurements for both transitions (see dashed curves in Fig. 4). We note that the simulated values of T_2 for the S_z transition appear below the experimental data points, and we assign this discrepancy to a small misalignment of our sample with respect to the magnetic field.

Our fourth observation concerns the T_2 behavior as $\partial f/\partial B_0$ approaches zero in the S_z transitions [Fig. 4(b)]. A key factor that distinguishes these measurements from those performed on a clock transition of Bi donors in natural silicon [14] is that here $\partial f/\partial B_0 \to 0$ coincides with the static magnetic field B_0 approaching zero [see Fig. 1(c)]. Therefore, rather than seeing the T_2 toward ~100 ms (as for Bi:^{nat}Si), the CCE-2 calculations predict an (orientation-dependent) limit of 1–2.5 ms. This can be understood as a "melting" of the "frozen core" of ^{29}Si spins around the donor spin, leading to enhanced noise from the spin bath. Furthermore, our measurements reveal an additional decrease in the fitted T_2 at the very lowest values of $\partial f/\partial B_0$ corresponding to $B_0 \lesssim 4$ mT, which we ascribe to periodic electron spin echo envelope modulation (ESEEM) from ^{29}Si nuclei in the crystal matrix. Simulations of the ESEEM performed using EASYSPIN [37] accounting for this are presented in the Supplemental Material [19], and the same effect has been observed recently in Bi:Si [38].

The measured coherence times of the near-surface $^{125}Te^+$ spins are about an order of magnitude longer compared to other spin centers at similar depths [16–18] with clear prospects of further improvement, as each of the limiting decoherence processes described above can be mitigated by moving to isotopically purified silicon [2,10,15,39]. Use of ^{28}Si should also substantially reduce the linewidths by removing the broadening from unresolved SHF levels. A better sample alignment and single-shot measurements can be achieved using superconducting resonators patterned onto implanted silicon [2,32].

In addition, the large (3.5 GHz) zero-field splitting of $^{125}Te^+$ makes it suitable for use at low magnetic fields and thus compatible with field-intolerant systems such as superconducting qubits. The nuclear spin half of ^{125}Te gives this donor an attractive level structure that can be used, for example, in so-called "flip-flop" qubits [5], and which permits near-complete polarization at dilution fridge temperatures, even at zero field. The significant second ionization energy permits the placement of spin-active $^{125}Te^+$ very close to surfaces and interfaces, which is beneficial for achieving large inductive coupling to microwave circuits [3]. All of these features, combined with the optical transitions of such donors [39], open a host of potential applications in quantum frequency converters, quantum sensors [40], and quantum memories.

In conclusion, our results show that $^{125}Te^+$ in silicon is a promising donor for use in quantum technology applications. We have demonstrated spin coherence times in excess of 1 ms, for donors at depths of only 20 nm from the surface, and in an isotopically purified ^{28}Si substrate these may be expected to become even longer. We have also shown a novel approach to ionize shallowly implanted chalcogens in nanoelectronic devices using surface band bending, which, when combined with infrared illumination, gives a single ionization fraction substantially greater than that achieved by codoping with acceptors, and no visible reduction in coherence time in natural silicon.

This work was supported by the UK EPSRC Skills Hub in Quantum Systems Engineering: Innovation in Quantum Business, Applications, Technology, and Engineering (InQuBATE), Grant No. EP/P510270/1; The European Research Council (ERC) via the LOQOMOTIONS grant (H2020-EU.1.1., Grant No. 771493). R. B. L. was supported by Hong Kong Research Grants Council General Research Fund Project 14302121, and S. L. was supported by The Chinese University of Hong Kong Impact Postdoctoral Fellowship. The authors acknowledge the UK National Ion Beam Centre (UKNIBC), where the silicon samples were ion implanted, and Nianhua Peng who performed the ion implantation.

M. S., J. O.-S., and O. W. K. contributed equally to this work.

---

*Corresponding author.
jjl.morton@ucl.ac.uk

[1] J. J. Pla, K. Y. Tan, J. P. Dehollain, W. H. Lim, J. J. Morton, D. N. Jamieson, A. S. Dzurak, and A. Morello, Nature (London) **489**, 541 (2012).

[2] V. Ranjan, J. O'Sullivan, E. Albertinale, B. Albanese, T. Chanelière, T. Schenkel, D. Vion, D. Esteve, E. Flurin, J. J. L. Morton, and P. Bertet, Phys. Rev. Lett. **125**, 210505 (2020).

[3] V. Ranjan, S. Probst, B. Albanese, T. Schenkel, D. Vion, D. Esteve, J. Morton, and P. Bertet, Appl. Phys. Lett. **116**, 184002 (2020).

[4] M. Urdampilleta, A. Chatterjee, C. C. Lo, T. Kobayashi, J. Mansir, S. Barraud, A. C. Betz, S. Rogge, M. F. Gonzalez-Zalba, and J. J. L. Morton, Phys. Rev. X **5**, 031024 (2015).

[5] G. Tosi, F. A. Mohiyaddin, V. Schmitt, S. Tenberg, R. Rahman, G. Klimeck, and A. Morello, Nat. Commun. **8**, 450 (2017).

[6] J. J. Pla, A. Bienfait, G. Pica, J. Mansir, F. A. Mohiyaddin, Z. Zeng, Y.-M. Niquet, A. Morello, T. Schenkel, J. J. L. Morton, and P. Bertet, Phys. Rev. Applied **9**, 044014 (2018).

[7] W. M. Witzel, M. S. Carroll, A. Morello, Ł. Cywiński, and S. Das Sarma, Phys. Rev. Lett. **105**, 187602 (2010).

[8] R. E. George, W. Witzel, H. Riemann, N. V. Abrosimov, N. Nötzel, M. L. W. Thewalt, and J. J. L. Morton, Phys. Rev. Lett. **105**, 067601 (2010).

[9] H. G. Grimmeiss, E. Janzén, H. Ennen, O. Schirmer, J. Schneider, R. Wörner, C. Holm, E. Sirtl, and P. Wagner, Phys. Rev. B **24**, 4571 (1981).

[10] R. Lo Nardo, G. Wolfowicz, S. Simmons, A. M. Tyryshkin, H. Riemann, N. V. Abrosimov, P. Becker, H.-J. Pohl, M. Steger, S. A. Lyon, M. L. W. Thewalt, and J. J. L. Morton, Phys. Rev. B **92**, 165201 (2015).

[11] G. Ludwig, Phys. Rev. **137**, A1520 (1965).

[12] A. DeAbreu, C. Bowness, R. J. S. Abraham, A. Medvedova, K. J. Morse, H. Riemann, N. V. Abrosimov, P. Becker, H.-J. Pohl, M. L. W. Thewalt, and S. Simmons, Phys. Rev. Applied **11**, 044036 (2019).

[13] J. Niklas and J. Spaeth, Solid State Commun. **46**, 121 (1983).

[14] G. Wolfowicz, A. M. Tyryshkin, R. E. George, H. Riemann, N. V. Abrosimov, P. Becker, H.-J. Pohl, M. L. Thewalt, S. A. Lyon, and J. J. Morton, Nat. Nanotechnol. **8**, 561 (2013).

[15] V. Ranjan, B. Albanese, E. Albertinale, E. Billaud, D. Flanigan, J. J. Pla, T. Schenkel, D. Vion, D. Esteve, E. Flurin, J. J. L. Morton, Y. M. Niquet, and P. Bertet, Phys. Rev. X **11**, 031036 (2021).

[16] D. Bluvstein, Z. Zhang, C. A. McLellan, N. R. Williams, and Ania C. Bleszynski Jayich, Phys. Rev. Lett. **123**, 146804 (2019).

[17] J. Wang, W. Zhang, J. Zhang, J. You, Y. Li, G. Guo, F. Feng, X. Song, L. Lou, W. Zhu, and G. Wang, Nanoscale **8**, 5780 (2016).

[18] R. Fukuda *et al.*, New J. Phys. **20**, 083029 (2018).

[19] See Supplemental Material at http://link.aps.org/supplemental/10.1103/PhysRevLett.129.117701 for additional information on the sample preparation, experimental details, spin Hamiltonian, simulations, and ESR experiments, which includes Refs. [20–24].

[20] J. F. Ziegler, M. D. Ziegler, and J. P. Biersack, Nucl. Instrum. Methods Phys. Res., Sect. B **268**, 1818 (2010).

[21] M. Šimėnas, J. O'Sullivan, C. W. Zollitsch, O. Kennedy, M. Seif-Eddine, I. Ritsch, M. Hülsmann, M. Qi, A. Godt, M. M. Roessler *et al.*, J. Magn. Reson. **322**, 106876 (2021).

[22] T. Schenkel, C. Lo, C. Weis, A. Schuh, A. Persaud, and J. Bokor, Nucl. Instrum. Methods Phys. Res., Sect. B **267**, 2563 (2009).

[23] A. Schweiger and G. Jeschke, *Principles of Pulse Electron Paramagnetic Resonance* (Oxford University Press on Demand, New York, 2001).

[24] A. M. Tyryshkin, S. Tojo, J. J. Morton, H. Riemann, N. V. Abrosimov, P. Becker, H.-J. Pohl, T. Schenkel, M. L. Thewalt, K. M. Itoh *et al.*, Nat. Mater. **11**, 143 (2012).

[25] J. J. Bollinger, J. D. Prestage, W. M. Itano, and D. J. Wineland, Phys. Rev. Lett. **54**, 1000 (1985).

[26] A. Ortu, A. Tiranov, S. Welinski, F. Fröwis, N. Gisin, A. Ferrier, P. Goldner, and M. Afzelius, Nat. Mater. **17**, 671 (2018).

[27] K. J. Morse, P. Dluhy, J. Huber, J. Z. Salvail, K. Saeedi, H. Riemann, N. V. Abrosimov, P. Becker, H.-J. Pohl, S. Simmons *et al.*, Phys. Rev. B **97**, 115205 (2018).

[28] D. Vion, A. Aassime, A. Cottet, P. Joyez, H. Pothier, C. Urbina, D. Esteve, and M. H. Devoret, Science **296**, 886 (2002).

[29] D. C. Gleason-Rohrer, B. S. Brunschwig, and N. S. Lewis, J. Phys. Chem. C **117**, 18031 (2013).

[30] I.-H. Tan, G. Snider, L. Chang, and E. Hu, J. Appl. Phys. **68**, 4071 (1990).

[31] K. Dev, M. Y. L. Jung, R. Gunawan, R. D. Braatz, and E. G. Seebauer, Phys. Rev. B **68**, 195311 (2003).

[32] J. O'Sullivan, O. W. Kennedy, C. W. Zollitsch, M. Šimėnas, C. N. Thomas, L. V. Abdurakhimov, S. Withington, and J. J. L. Morton, Phys. Rev. Applied **14**, 064050 (2020).

[33] T. Sekiguchi, A. Tyryshkin, S. Tojo, E. Abe, R. Mori, H. Riemann, N. Abrosimov, P. Becker, H.-J. Pohl, J. Ager *et al.*, Phys. Rev. B **90**, 121203(R) (2014).

[34] W. Yang and R.-B. Liu, Phys. Rev. B **78**, 085315 (2008).

[35] E. Abe, A. M. Tyryshkin, S. Tojo, J. J. Morton, W. M. Witzel, A. Fujimoto, J. W. Ager, E. E. Haller, J. Isoya, S. A. Lyon *et al.*, Phys. Rev. B **82**, 121201(R) (2010).

[36] P. Ross, B. C. Rose, C. C. Lo, M. L. W. Thewalt, A. M. Tyryshkin, S. A. Lyon, and J. J. L. Morton, Phys. Rev. Applied **11**, 054014 (2019).

[37] S. Stoll and A. Schweiger, J. Magn. Reson. **178**, 42 (2006).

[38] S. Probst, G. Zhang, M. Rančić, V. Ranjan, M. Le Dantec, Z. Zhang, B. Albanese, A. Doll, R. B. Liu, J. Morton, T. Chanelière, P. Goldner, D. Vion, D. Esteve, and P. Bertet, Magn. Reson. **1**, 315 (2020).

[39] K. J. Morse, R. J. S. Abraham, A. DeAbreu, C. Bowness, T. S. Richards, H. Riemann, N. V. Abrosimov, P. Becker, H.-J. Pohl, M. L. W. Thewalt, and S. Simmons, Sci. Adv. **3**, e1700930 (2017).

[40] J. R. Maze, P. L. Stanwix, J. S. Hodges, S. Hong, J. M. Taylor, P. Cappellaro, L. Jiang, M. G. Dutt, E. Togan, A. Zibrov *et al.*, Nature (London) **455**, 644 (2008).